A global map of Mars' crustal magnetic field based on electron reflectometry

D. L. Mitchell,[1] R. J. Lillis,[1] R. P. Lin,[1] J. E. P. Connerney,[2] and M. H. Acuña[2]

Received 24 August 2005; revised 5 May 2006; accepted 2 August 2006; published 9 January 2007.

[1] We present a global map of the amplitude of Mars' crustal magnetic field at 170-km altitude based on electron reflectometry, using data from the Magnetometer/Electron Reflectometer (MAG/ER) experiment on board Mars Global Surveyor. This new map contains features that are about seven times weaker than those in previously published maps obtained with the MAG alone from the 400-km-altitude mapping orbit. The increased sensitivity and nearly complete sampling reveal numerous weak magnetic sources in the northern lowlands. A group of these sources forms a nearly complete ring surrounding the Utopia basin, coinciding with a ridge of thickened crust. A larger 5800-km-diameter ring is defined by a $\sim$120° arc of magnetic sources that extend to the north pole, supporting the hypothesis that part of the dichotomy boundary was established or modified by the Utopia impact. We also map the magnetic signatures of the Hellas, Argyre, and Isidis impact basins with increased dynamic range, confirming the large contrast in magnetic field strength between the basin interior and surroundings. Magnetic sources surround most of the Tharsis rise, except in the north, suggesting that the construction of Tharsis thermally demagnetized a large region of the northern lowlands. Thermal demagnetization is also suggested in the Elysium region, which intersects the inner Utopia magnetic ring, and south of the Hellas basin in the vicinity of Peneus Patera and Amphitrites Patera.

Citation: Mitchell, D. L., R. J. Lillis, R. P. Lin, J. E. P. Connerney, and M. H. Acuña (2007), A global map of Mars' crustal magnetic field based on electron reflectometry, *J. Geophys. Res.*, *112*, E01002, doi:10.1029/2005JE002564.

1. Introduction

[2] One of the great surprises of the Mars Global Surveyor (MGS) mission was the discovery of intensely magnetized crust [*Acuña et al.*, 1999]. The strongest crustal fields are associated with the oldest terrain on Mars and have corresponding magnetic moments estimated to be at least ten times stronger than their terrestrial counterparts, probably requiring large volumes of coherently magnetized material, very strong remanence, or both [*Connerney et al.*, 1999]. There is no evidence for significant magnetic fields within the Hellas and Argyre basins [*Acuña et al.*, 1999; *Connerney et al.*, 2001], most likely because of shock/thermal demagnetization from the impacts that formed these basins. Thus Mars' crustal magnetic fields are preserved in some of the oldest geologic features on the planet.

[3] Although much of the attention so far has been placed on the strong crustal fields south of the dichotomy, magnetic sources do exist in the northern low-lying plains. The strength and morphology of these sources could yield clues to the northern plains' thermal and magnetic histories. Low-altitude ($\sim$100–150 km) magnetometer data obtained during aerobraking provide the most sensitive means for identifying crustal magnetic sources from orbit, but those data are sparse ($\sim$20% coverage [*Acuña et al.*, 1999]) and were obtained almost entirely on the sunlit hemisphere, where variable $\sim$30-nT external fields due to the solar wind/ionosphere interaction obscure weak crustal sources. Magnetometer data obtained on the night hemisphere at the mapping altitude ($\sim$400 km) are fully sampled, but crustal sources produce signal amplitudes at 400 km that are about an order of magnitude smaller than those at 150 km. Differentiating the radial component of the magnetic field along the orbit track reduces the influence of external fields due to the solar wind interaction (since external fields typically have much larger radii of curvature than fields from crustal sources) and thus enhances the sensitivity to crustal sources [*Connerney et al.*, 2005]. The electron reflection method described here represents an independent search for weak crustal fields that complements the differentiated magnetometer data.

[4] Electron reflectometry takes advantage of the magnetic mirror effect, specifically, the reflection of solar wind electrons from regions of increasing magnetic field strength. In a uniform field, electrons gyrate around magnetic field lines on helical paths of constant radius and pitch angle (α), which is the angle between an electron's velocity and the magnetic field. On field lines connected to crustal magnetic sources, the field strength (B) increases toward the planet, while the fractional change in the field is small over the

[1]Space Sciences Laboratory, University of California, Berkeley, California, USA.
[2]NASA Goddard Space Flight Center, Greenbelt, Maryland, USA.

0148-0227/07/2005JE002564

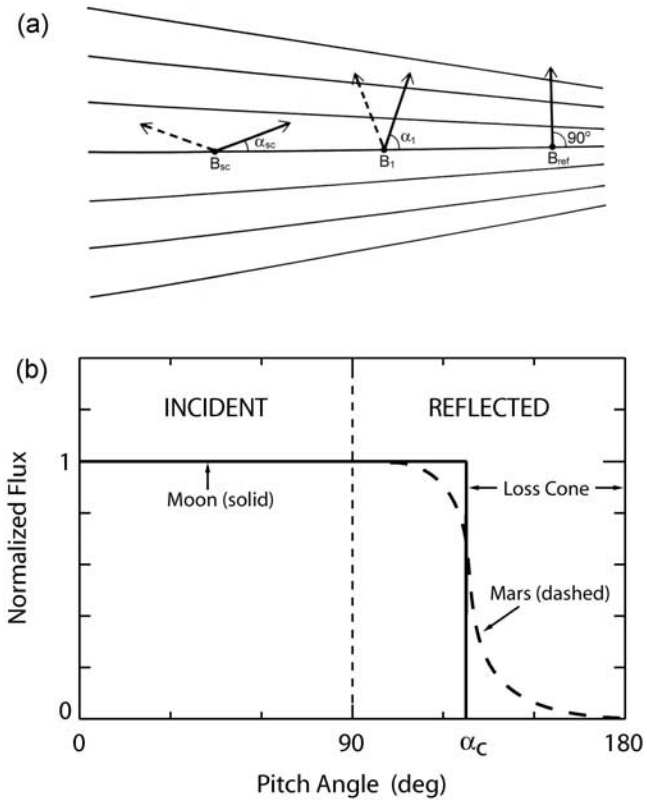

Figure 1. (a) Instantaneous velocity vectors for an electron traveling along converging magnetic field lines between the spacecraft and the reflection point (solid vectors are incident, and dashed vectors are reflected). As the electron travels toward increasing magnetic field strength, its pitch angle (α) satisfies $B/\sin^2\alpha$ = constant. The electron is reflected back toward the spacecraft when α reaches 90°, and $B_{ref} = B_{sc}/\sin^2\alpha_{sc}$. (b) Electron pitch angle distribution measured at the spacecraft. For the Moon (solid line) the loss cone is formed at the surface, resulting in a sharply defined cutoff pitch angle (α_C). For Mars (dashed line) the loss cone is formed in the atmosphere from ~150- to 300-km altitude. The loss cone is modeled to determine the relationship between pitch angle and altitude.

distance traveled by an electron in one gyration. (Below 400-km altitude on Mars' night hemisphere, where B > 10 nT, this distance is less than 30 km for 200-eV electrons. The corresponding radius of gyration for these electrons is less than 3.4 km.) Under these conditions, the adiabatic approximation holds ($\sin^2\alpha/B$ = constant), and electrons are reflected back along the lines of force if α reaches 90° (Figure 1a). If there is no interaction with the atmosphere, then downward traveling electrons with a pitch angle of α_{sc} at the spacecraft return after a round-trip time of ~0.1 s with a pitch angle of $180° - \alpha_{sc}$.

[5] At the Moon, which has a negligible atmosphere, incident electrons with α_{sc} between 90° and some critical value (α_c) are reflected before they reach the surface and return to the spacecraft without attenuation (Figure 1b). Incident electrons with $\sin(\alpha_{sc}) < \sin(\alpha_c)$ impact the surface, where they are nearly completely absorbed. Using the adiabatic condition, the surface magnetic field strength can be determined from measurements of B_{sc} and α_c at the spacecraft: $B_{surf} = B_{sc}/\sin^2\alpha_c$. Since the loss cone is sharply defined, and α_c corresponds to reflection at a known altitude (0 km), detailed knowledge of the interaction between electrons and the lunar surface is unnecessary.

[6] At Mars, electrons are absorbed by the atmosphere over a range of altitudes, and the loss cone is no longer defined by a sharp edge (Figure 1b). Since the magnetic field strength increases monotonically toward the surface, there is a one-to-one mapping between α_{sc} and reflection altitude: Downward traveling electrons with $\alpha_{sc} \approx 90°$ reflect at high altitudes, while those with smaller values of $\sin(\alpha_{sc})$ reflect at lower altitudes. The atmospheric density increases exponentially toward the surface [*Nier and McElroy*, 1976], so the probability that an electron will impact a neutral species increases rapidly as the reflection point gets lower. Most scattered electrons do not return to the spacecraft, so the flux of upward traveling electrons exhibits an attenuation that depends sensitively on α_{sc} (Figure 1b). Modeling of the interaction between electrons and the atmosphere is required to determine the relationship between the amount of attenuation and reflection altitude.

[7] Precipitating solar wind electrons collide with neutral atoms and molecules, transferring their kinetic energy primarily into excitation and ionization of CO_2 and O. Some of these scattered electrons return to the spacecraft and modify the shape of the loss cone; however, the pitch angle distribution of backscattered electrons is distinct from that of magnetically reflected electrons, which allows separation of the two components [*Lillis et al.*, 2004]. The fraction of the incident flux that is magnetically reflected back to the spacecraft is given by the probability, P, that an electron can avoid collisions with atmospheric neutrals along a helical trajectory of length L from the spacecraft to the reflection point and back:

$$P = 1 - \exp\left[-\sum_i \int_0^L \sigma_i n_i(s) ds\right], \quad (1)$$

where n_i and σ_i are the densities and total collision cross sections of the various atmospheric constituents, and s is distance along the helical path. Electron impact cross sections are taken from *Sung and Fox* [2000], and we adopt a nighttime (3 am local time) thermospheric density/composition profile based on the Mars Thermospheric Global Circulation Model (MTGCM [*Bougher et al.*, 1990, 1999, 2000]), extrapolated to the spacecraft altitude assuming diffusive equilibrium above the exobase. Although the thermospheric density is expected to vary with the Sun-Mars distance and solar activity, we choose a fixed average density profile and incorporate variations (as predicted by the MTGCM) into our uncertainty estimate.

[8] To calculate the helical path, we assume the magnetic field is a straight line from the spacecraft down to electron absorption altitudes, with a direction given by the magnetic field vector measured at the spacecraft. We write the magnetic field amplitude along this line as the sum of a constant external field (B_{sw}) and a power law due to crustal sources:

$$B(x) = B_{sw} + (B_{sc} - B_{sw})\left(\frac{x_s}{x}\right)^a, \quad (2)$$

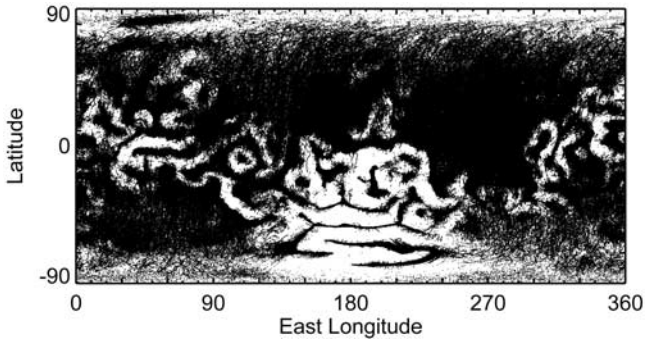

Figure 2. Each electron reflection measurement used in this study, represented by a black dot. Where the crustal field is weak, dense sampling is obtained within 60° of the equator. The sampling is less dense at higher latitudes, where the draped interplanetary magnetic field (IMF) often makes an angle of less than 30° with respect to the local horizontal. Measurements on such field lines are not included in this study (see text). Where the crustal field is strong, measurements are confined to field lines with relatively large radial components that can connect to the IMF (magnetic "cusps").

where B_{sc} is the field strength measured at the spacecraft, and x_s is the distance along the field line from the spacecraft to the magnetic source region, assumed to be 15 km below the surface, or about half the depth of the magnetized layer, as estimated by *Nimmo and Gilmore* [2001]. We adopt a power law exponent of $a = 2.5$ as a compromise between an infinite line of dipoles ($a = 2$) and an isolated dipole ($a = 3$). The effective power law exponent over the strong magnetic sources in Terra Sirenum, for example, is ~2.2 [*Brain et al.*, 2003]. This choice is not critical, as sensitivity tests show that estimates of the magnetic field amplitude in the electron absorption region are relatively insensitive to the exponent over the range of 2 to 3.

[9] The fitting procedure consists of first subtracting the backscatter population from the measured pitch angle distribution and then adjusting B_{sw} to provide the best agreement between P and the pitch angle distribution of magnetically reflected electrons. The crustal field amplitude at altitudes where the loss cone is formed (~150 to 300 km for 200-eV electrons) is then calculated from equation (2). For convenience, we present our results in terms of B_{170}, or the crustal magnetic field amplitude at 170-km altitude. Altitude is defined with respect to the gravitational equipotential surface that has a mean equatorial radius of 3396 km [*Smith et al.*, 2001].

2. Data

[10] The MGS Electron Reflectometer (ER) is a hemispherical imaging electrostatic analyzer that measures the local electron population's distribution in energy and angle [*Mitchell et al.*, 2001]. Electron fluxes are measured in sixteen 22.5° × 14° sectors spanning a 360° × 14° field of view (FOV), and in 19 logarithmically spaced energy channels ranging from 0.01 to 20 keV, with an energy resolution of $\Delta E/E = 0.25$ (full width at half maximum). For this study, we use the 191-eV channel (spanning 143–239 eV), where the count rate is high and the effects of spacecraft charging are negligible. With knowledge of the local magnetic field vector measured onboard, the FOV is mapped into pitch angle. During a 2- to 8-s integration, the ER measures between 8% and 100% of the 0°–180° pitch angle spectrum, depending on the orientation of the magnetic field with respect to the FOV plane. The large volume of mapping orbit data contains $>2 \times 10^6$ spectra with sufficient pitch angle coverage for analysis.

2.1. Coverage and Sampling

[11] All data used in this study were obtained in the ~400-km-altitude mapping orbit on the night hemisphere (~2 am local time). In this region, the external field is dominated by the draped interplanetary magnetic field (IMF), which has an amplitude of ~10 nT and is roughly aligned with the Sun-Mars line [*Ferguson et al.*, 2005]. The gradient in the external field from 400- to 150-km altitude is small enough that it does not produce a measurable reflected electron population (α_c is indistinguishable from 90°). Thus we attribute any upward traveling electrons to reflection from crustal magnetic fields. To map field lines from the spacecraft altitude to lower altitudes, we start with the field vector measured at the spacecraft by the MGS Magnetometer (MAG) and assume that it continues in a straight line down to 150-km altitude. This is a good approximation where the field at the spacecraft is dominated by the draped IMF, but field line curvature associated with strong crustal sources will cause errors that increase with distance from the spacecraft. To minimize these errors, we restrict the map to field lines that make an angle of at least 30° to the local horizontal, corresponding to a maximum distance between the spacecraft and the reflection point of ~500 km.

[12] Our technique can only probe crustal magnetic field lines that are connected to the IMF ("open"), so that solar wind electrons make a single round trip through the atmosphere, from the spacecraft to the reflection point and back. This means that there will necessarily be nonuniform sampling of the crustal magnetic field (Figure 2). Over strong crustal sources (e.g., 140°–240°E in the southern hemisphere) field lines with a large radial component tend to connect with the IMF often, whereas nearby field lines with a more horizontal orientation at 400-km altitude rarely (or never) connect with the IMF. Because electrons are trapped on such field lines and can mirror through the atmosphere multiple times, our technique for constraining the field strength does not apply. Nevertheless, pitch angle distributions readily reveal the presence of such closed field lines. Since the crustal fields rotate with the planet and the IMF changes direction, magnetic field topology should be dynamic, but since we are using a large volume of data spanning more than two Martian seasons, we can map field lines that are open only part of the time.

2.2. Construction of the Map

[13] The data used to construct the ER map consist of least-squares fits to 2×10^6 pitch angle distributions, each yielding an estimate of B_{170}. These are mapped from the spacecraft to 170-km altitude using a straight line approximation, as described above. The values of B_{170} are then averaged in 150-km-diameter resolution elements, or cells, as follows. We start with a 150-km-diameter circle in the

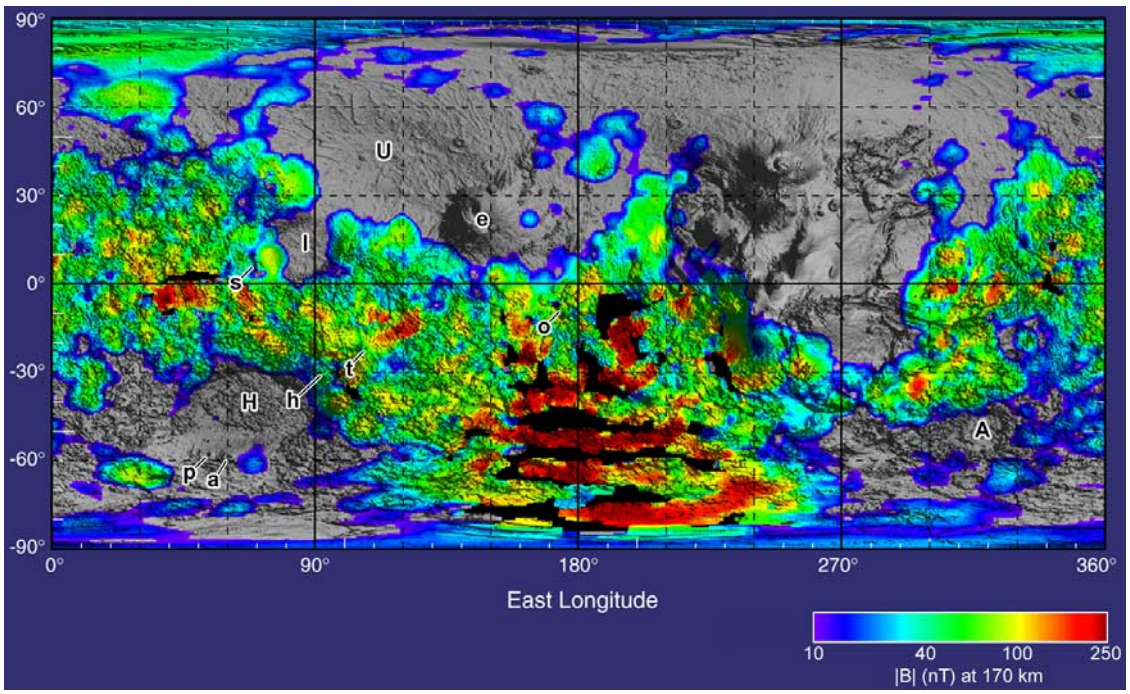

Figure 3. The crustal magnetic field amplitude at an altitude of 170 km (B_{170}), as inferred from electron reflectometry, represented as colors superimposed on a shaded relief map of MGS Mars Orbiter Laser Altimeter topography. Gray scale regions have $B_{170} < 10$ nT. Crustal magnetic field lines form closed loops in black regions, where the Electron Reflectometer (ER) method cannot be used (see text). Labels indicate the centers of the Utopia (U), Hellas (H), Argyre (A), and Isidis (I) impact basins, as well as the volcanoes Elysium (e), Syrtis Major (Nili and Meroe) (s), Apollinaris (o), Tyrrhena (t), Hadriaca (h), Peneus (p), and Amphitrites (a).

local horizontal plane with its center at 0° longitude and 0° latitude. The mean and standard deviation of all B_{170} measurements that fall within the circle are calculated. The circle is then moved by 0.5° in longitude or latitude, and new values of the mean and standard deviation are calculated. This is repeated until the center of the circle visits all positions on the sphere (with 0.5° granularity). The final map has a 150-km resolution that is oversampled with 0.5° pixels. This resolution should be sufficient to follow variations in the crustal magnetic field strength, which we expect to be dominated by scale lengths comparable to or greater than the reference altitude of 170 km [*Connerney et al.*, 2004].

[14] Figure 3 shows B_{170} as color superimposed on a shaded relief map derived from MOLA topography. The maximum field strength shown is 250 nT, although peak values of B_{170} exceed 1000 nT. This was done to highlight relatively weak fields and because stronger fields are well mapped by the MAG at 400-km altitude [*Acuña et al.*, 2001; *Connerney et al.*, 2001]. Regions without superimposed color are composed of cells with good sampling but for which the average value of B_{170} is less than 10 nT (see below). Black regions are composed of cells with insufficient sampling (0 or 1 measurement), which occur where crustal field lines are rarely or never connected to the IMF, even though the field strength may be significant.

[15] The uncertainty in B_{170} from fitting an individual pitch angle distribution is typically ~30%, which is compatible with the standard deviation of measurements within mapping cells (Figure 4a). This demonstrates that the uncertainty in estimating B_{170} is dominated by known errors in the fitting procedure. Distributions of B_{170} in the weakest regions show standard deviations of ~2 nT (Figure 4c), which we take to be indistinguishable from zero. This is five times smaller than our mapping threshold of 10 nT and places an upper limit on magnetic field gradients in the draped IMF. The uncertainty increases for $B_{170} > 300$ nT, because the loss cone forms closer to 0° or 180°, where the location of the loss cone is relatively insensitive to changes in the field strength. The highest measured values of B_{170} exceed 1000 nT, for which the uncertainty is about a factor of two.

[16] More than two Martian seasons of mapping orbit data (April 1999–November 2003) provide sufficient sampling over much of the planet to test the repeatability of the measurements. We divided the mapping orbit data in half and created two independent ER maps, as described above, and then differenced them. All of the features in Figure 3 are reproduced in both maps to within 30% (Figure 4b), which is consistent with known uncertainties in the fitting procedure.

3. Discussion

3.1. Comparison With Previous Results

[17] The spatial distribution of features in our B_{170} map agrees well with previously published maps based on MGS Magnetometer measurements at ~400-km altitude on the

night hemisphere [*Acuña et al.*, 2001; *Connerney et al.*, 2001]. All of the features in the Magnetometer maps stronger than 10 nT (at 400 km) have corresponding features at the same locations in the B_{170} map. To make a quantitative assessment, we compare B_{170} to estimates of the magnetic field amplitude based on downward continuation of the MAG data to 170-km altitude. For this purpose, we use the spherical harmonic expansion of *Cain et al.* [2003] (hereinafter referred to as the "Cain model") evaluated at 170-km altitude and smoothed with a 150-km-diameter circle in the same way as the ER map. Some longitude/latitude misalignment between the downward continued Cain model (B_C) and B_{170} is expected because the former includes field line curvature whereas the latter uses a straight line approximation between 400- and 170-km altitude. We restrict the comparison to regions where $B_{170} >$ 100 nT, corresponding to crustal field amplitudes greater than ~13 nT at the mapping orbit (assuming the field strength varies with altitude according to equation (2)). In these regions, crustal field amplitudes in the ER map are generally compatible with estimates based on downward continuation of the MAG data (Figure 4d). The largest values of $B_{170} - B_C$, particularly those in the non-Gaussian tail of the distribution, occur mostly in the Terra Sirenum region, where the field strength is large and field line curvature is significant.

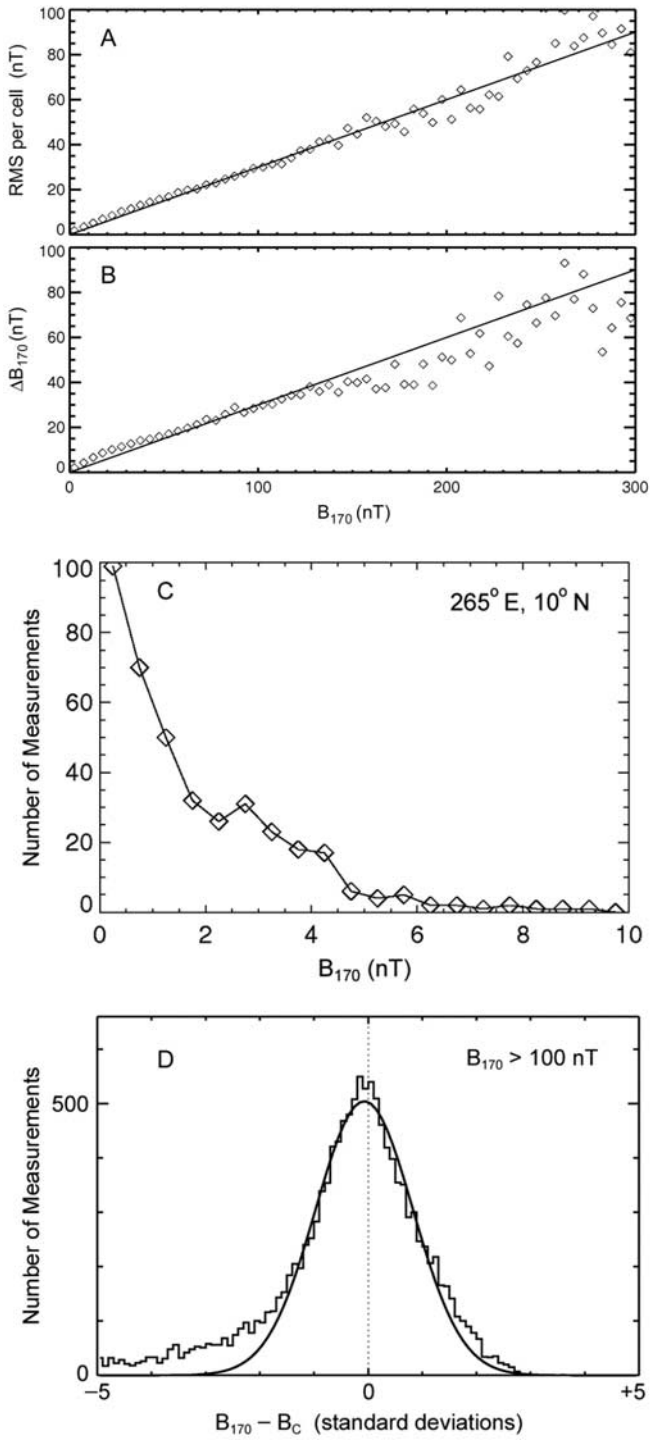

Figure 4. (a) Plot showing that the standard deviation of B_{170} within 150-km-diameter cells is proportional to the mean value of B_{170} over a wide range. (b) Plot showing that the differences between two maps of B_{170} constructed with independent subsets of the data are also roughly proportional to B_{170}. In both Figures 4a and 4b the solid line shows 30% of B_{170}. (c) The distribution of B_{170} values within a 150-km-diameter region centered on 265°E, 10°N (600 km east of Ascraeus Mons), with a mean of 1.9 nT, a median of 1.3 nT, and a standard deviation of 2.1 nT. (d) Histogram showing the distribution of differences between B_{170} and the amplitude of a spherical harmonic expansion of the crustal magnetic field evaluated at 170-km altitude (B_C [*Cain et al.*, 2003]). Only measurements where $B_{170} >$ 100 nT are included in the distribution. A Gaussian for which the standard deviation is 30% of B_{170} is shown for comparison (smooth curve).

3.2. Impact Basins

[18] The first global magnetic map of Mars [*Acuña et al.*, 1999] revealed that the Hellas and Argyre impact basins were regions of weak magnetic fields, most likely as a result of impact demagnetization, although this interpretation was challenged [*Schubert et al.*, 2000]. The higher sensitivity of the ER map allows us to more clearly define the magnetic signatures of these two basins (Figure 3). We find no evidence for crustal fields stronger than a few nT at 170 km (<1 nT at 400 km) within Hellas or Argyre. Furthermore, the distribution of crustal fields north of Hellas follows the basin perimeter, strongly supporting the hypothesis that the Hellas impact erased preexisting fields by thermal and/or shock demagnetization [*Acuña et al.*, 1999; *Hood et al.*, 2003; *Mohit and Arkani-Hamed*, 2004]. However, the distribution of magnetic sources is not symmetric about the basin center. Magnetic sources south of Hellas are weaker and do not closely follow the basin perimeter, although the region bordering the southwest rim of Hellas could have been thermally demagnetized long after the impact by magma intrusions associated with the middle-to-late Noachian volcanoes Peneus and Amphitrites. Magnetic sources around Argyre show a similar pattern, with stronger sources north of the basin. There is no evidence for magnetic sources west of Argyre, extending over 1000 km westward into Aonia Terra. The Isidis basin has the clearest magnetic signature, defined by a nearly circular region with

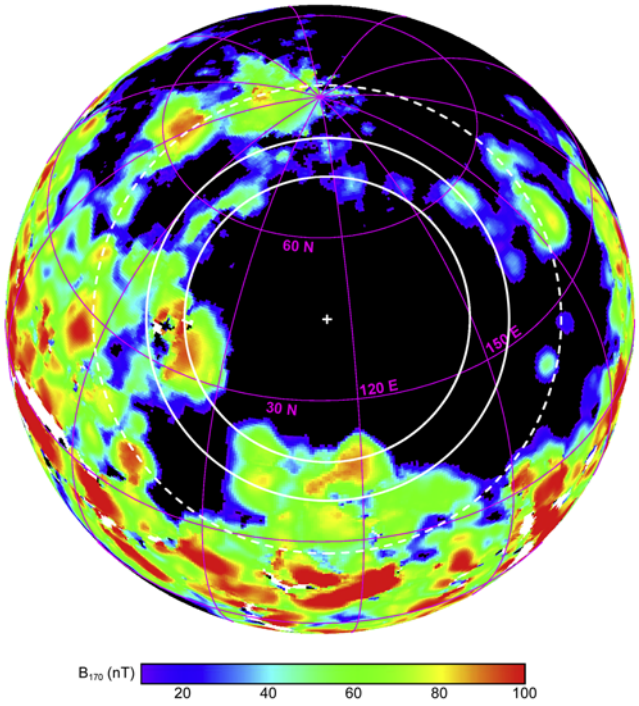

Figure 5. B_{170} shown in an orthographic projection. The Utopia basin center (pluses) and 3200-km-diameter inner ring are based on topographic data [*Thomson and Head*, 1999], while the 4070-km-diameter middle ring coincides with the dichotomy boundary from 70° to 120°E longitude [*Frey et al.*, 2002]. (The ring proposed earlier by *Schultz and Frey* [1990] is ~600 km larger because they adopted a basin center that was shifted ~300 km to the northeast.) The outer dashed ring, 5800 km in diameter, is defined by an arc of magnetic sources on the western side of the basin. Note the different color scale compared with Figure 3.

no detectable fields surrounded by prominent sources. Thus, while the demagnetization signatures of Hellas, Argyre, and Isidis are confirmed with a higher dynamic range, the distribution of magnetic sources in the highland terrain prior to these impacts was clearly nonuniform.

[19] The Utopia basin has been identified as an impact structure on the basis of geologic [*McGill*, 1989; *Head et al.*, 2002] and topographic [*Smith et al.*, 1999; *Thomson and Head*, 1999] evidence. The distribution of quasi-circular depressions (QCD's), interpreted as buried craters, within the basin suggests that it dates from the early Noachian [*Frey*, 2003], while the basin morphology and gravity signature indicate that it postdates the formation of the crustal dichotomy [*Neumann et al.*, 2004]. The ER map shows a partial ring of enhanced B_{170} values surrounding the Utopia basin (Figure 5). This magnetic ring lies just outside of the 3200-km-diameter main topographic rim and coincides with a ring of thickened crust identified from MGS gravity and altimetry [*Neumann et al.*, 2004]. The western half of the magnetic ring is nearly complete and symmetric about the basin center, here taken to be 114°E, 45°N [*Frey et al.*, 2002]. The ring continues in the northeast symmetrically about the basin center from 78°N to 60°N, but farther south, enhanced values of B_{170} begin to extend farther from the basin center, following a ridge of thickened crust instead of the topographic rim. The southeastern part of the ring is missing, although it could have been thermally demagnetized by the creation of the Elysium volcanic region.

[20] One possible interpretation is that the ring of magnetic sources around Utopia was formed by impact demagnetization of some preexisting distribution of magnetized crust. The survival of magnetic sources just outside of the main topographic rim would be consistent with the demagnetization signatures of Hellas and Argyre. However, the Utopia magnetic signature is unlike those for Hellas and Argyre in that it consists of a distinct magnetic annulus instead of a circular hole. An alternative interpretation is that the annulus of thickened crust marks the location of an inner ring that was remagnetized after the Utopia impact. A larger ring for the Utopia basin (Figure 5) has been proposed on the basis that it fits the dichotomy boundary from 70°E to 120°E [*Frey and Schultz*, 1988; *Schultz and Frey*, 1990]. If this ring is interpreted as the main rim, then the magnetic annulus would be at ~0.9 basin radii, where part of the crust could have been shock heated above the Curie temperature, depending on the identity of the magnetic carrier [*Mohit and Arkani-Hamed*, 2004]. This second interpretation would require that the core dynamo was active at the time of the Utopia impact, which predates both the Hellas and Argyre impacts based on visible and buried crater counts [*Frey*, 2004]. Both interpretations imply the presence of magnetized early Noachian crust in the northern lowlands beneath a much younger surface. This is compatible with the interpretation of *Frey et al.* [2002], that the northern lowlands preserve numerous buried impact craters, and that the smooth, young surface is only a thin (few kilometers) veneer covering crust that is nearly as old as the southern highlands [*Frey*, 2004].

[21] The correlation of the magnetic ring with a ridge of thickened crust introduces another interesting aspect to this signature. The huge magnetic moments associated with the strongest magnetic fields in the southern hemisphere [*Connerney et al.*, 1999] probably require volumes of magnetized crust that are tens of kilometers thick. Deep seated (~30–50 km) magnetic source regions are also inferred from the lack of demagnetization signatures for small craters [*Nimmo and Gilmore*, 2001; *Mohit and Arkani-Hamed*, 2004] and spectral analysis of the MGS magnetic field data [*Voorhies et al.*, 2002]. The weaker magnetic fields in the northern lowlands might then be at least partly explained by a thinner crust (~30 km compared with ~60 km in the highlands [*Neumann et al.*, 2004]), while variations in crustal thickness could result in observable magnetic signatures. Further support for this interpretation can be seen in the north polar region (Figure 6), where the two most prominent magnetic sources (the "north polar anomalies") coincide with a subdued ridge of thickened crust, while areas of thin crust tend to occur where B_{170} is weak. This correlation is not apparent in the southern highlands, where the crust is much thicker. For example, the ring of thickened crust surrounding the Hellas basin is much more pronounced than that for Utopia [*Neumann et al.*, 2004]; however the distribution of magnetic sources around Hellas does not follow this ring. In particular, no detectable magnetic fields are observed over a large area west of Hellas (centered at 30°E, 40°S; see Figure 3).

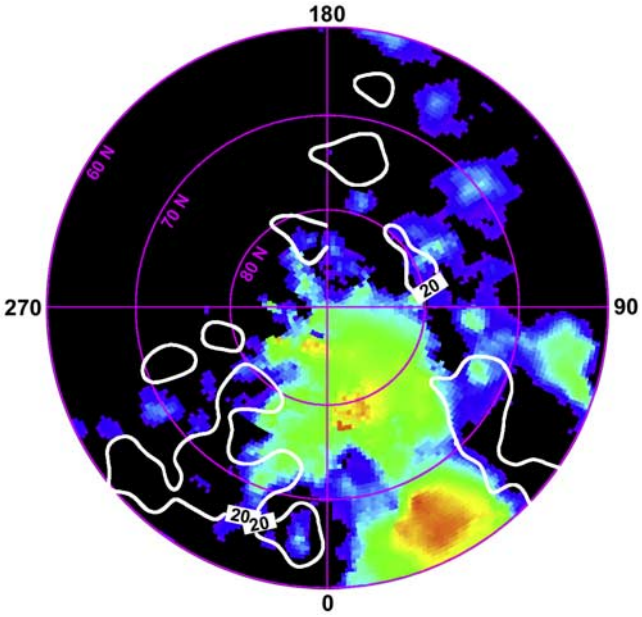

Figure 6. B_{170} shown in an orthographic projection centered on the north pole. White contours [from *Neumann et al.*, 2004] enclose regions where the crust is less than 20 km thick. See Figure 5 for the color scale.

[22] Finally, we note that the north polar anomalies form part of an arc of magnetic sources (Figure 5, dashed line) with a diameter of ~5800 km that is roughly concentric with the main topographic rim. This magnetic arc is composed of numerous sources west of Utopia, as well as a few in the east. If this magnetic feature is associated with Utopia, then it lends support to the presence of a 4070-km-diameter ring, and consequently to the hypothesis that part of the dichotomy boundary was formed or modified by the impact [*Frey and Schultz*, 1988; *Schultz and Frey*, 1990].

3.3. Volcanic Regions

[23] Gaps in the distributions of magnetic sources surrounding the Hellas and Utopia basins suggest the possibility of thermal demagnetization associated with volcanoes. Although surface lava flows and subsurface intrusions can cause demagnetization, their dimensions are typically too small (tens of meters [*McEwen et al.*, 1999; *Hiesinger and Head*, 2004; *Wilson and Head*, 1997]) to affect a significant fraction of the potentially magnetized region [*Johnson and Phillips*, 2005]. Thus, unless the magnetization is strongly concentrated near the surface, persistent heating from below over mantle hot spots and in the vicinity of large magma chambers are the most likely mechanisms for thermal demagnetization in the Martian crust.

[24] The Tharsis rise is the largest volcanic construct on Mars and also contains one of the largest regions with magnetic field amplitudes below our mapping threshold ($B_{170} < 10$ nT). The distribution of individual B_{170} measurements within this region reveals that the field strength is even below our detection threshold of a few nT (Figure 4c). Although most of the Tharsis rise has a very weak magnetic signature, its southernmost extent, including Daedalia Planum, Claritas Fossae, and Nectaris Fossae, contains several strong ($B_{170} > 90$ nT) crustal magnetic fields (Figure 7). Magnetic fields in southwestern Daedalia Planum are comparable in strength to those in neighboring Terra Sirenum, indicating that the construction of Tharsis did not greatly affect magnetized crust in that region. The sources for these fields are thought to be located in magnetized Noachian crust that has been uplifted and in some cases resurfaced, but only partially thermally demagnetized [*Johnson and Phillips*, 2005].

[25] Along the western and eastern borders of the Tharsis rise, strong magnetic sources extend northward to about 20°N, through Amazonis Planitia and Xanthe Terra, respectively. Much weaker magnetic sources continue northward on both sides of the Tharsis rise to about 50°N (Figure 7). The presence of magnetic sources surrounding all but the northern border of Tharsis strongly implies that the construction of Tharsis thermally demagnetized a large region of the northern lowlands. Demagnetization appears more complete in the lowlands, where the crust is thinner and magnetic fields are generally much weaker than in the southern highlands.

[26] The situation is less clear when considering volcanoes in the southern highlands. The magnetic field distribution contains many local maxima and minima throughout this region, so there is no way to confidently assess the preexisting magnetic field strength at any particular volcanic site. Nevertheless, B_{170} is below the mapping threshold at Peneus and Amphitrites Paterae, while Nili and Meroe Paterae (Syrtis Major) and Tyrrhena Patera (Hesperia) are situated at local minima (Figure 3), which is consistent with at least some thermal demagnetization at these locations. On the other hand, Hadriaca Patera ($B_{170} \approx 30$ nT) and Apollinaris Patera (in a closed field region where $B_{170} > 50$ nT) are not situated at local minima in the magnetic field amplitude, although this does not rule out the possibility that the crustal field at these sites was even stronger in the past. A more detailed analysis, which is beyond the scope of this paper, is needed to better interpret the magnetic signatures of highland volcanoes [see *Lillis et al.*, 2005].

4. Conclusion

[27] We have used electron reflectometry to create a global map of Mars' crustal magnetic field at 170-km altitude. The large-scale morphology of weak crustal magnetic sources in the northern lowlands reveals a ring surrounding the Utopia basin that likely originates from magnetized Noachian crust that survived the Utopia impact. This ring coincides with a ridge of thickened crust identified from MGS gravity and topography data. There is evidence for a much larger magnetic ring around Utopia, 5800 km in diameter, which supports the hypothesis that the Utopia impact formed or modified part of the dichotomy boundary.

[28] The magnetic field amplitude throughout most of the Tharsis rise is at or below our detection threshold of a few nT at 170-km altitude. Strong magnetic sources are present in the southernmost regions of Tharsis, while weaker sources extend along its entire western and eastern borders, which strongly implies that the construction of Tharsis thermally demagnetized a large region of the planet. Gaps in the distributions of magnetic sources surrounding the Utopia and Hellas basins also suggest the possibility of thermal demagnetization associated with Elysium Mons and

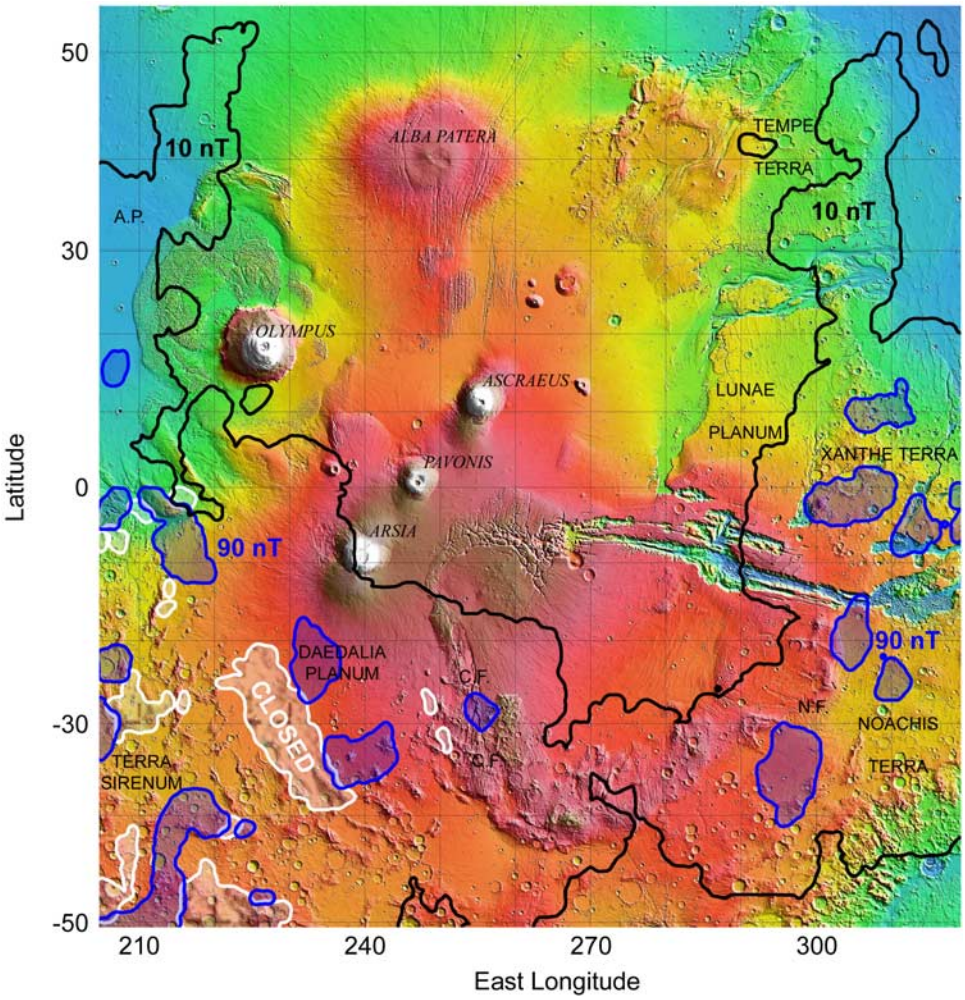

Figure 7. Contours of B_{170} superimposed on a topographic map of the Tharsis rise from the MGS MOLA experiment. Contours at B_{170} = 10 nT and 90 nT are shown in black and blue, respectively. Regions where the magnetic field is strong but not connected to the IMF ("closed") are outlined in white. C.F., Claritas Fossae; N.F., Nectaris Fossae; A.P., Amazonis Planitia.

Peneus and Amphitrites Paterae; however, the magnetic signatures of highland volcanoes are difficult to interpret because of the structured magnetic field distribution throughout the southern hemisphere.

[29] **Acknowledgments.** This work was supported by NASA grant NNG04GL35G and JPL contract 1271721.

References

Acuña, M. H., et al. (1999), Global distribution of crustal magnetization discovered by the Mars Global Surveyor MAG/ER experiment, *Science*, *284*, 790–793.

Acuña, M. H., et al. (2001), The magnetic field of Mars: Summary of results from the aerobraking and mapping orbits, *J. Geophys. Res.*, *106*, 23,403–23,418.

Bougher, S. W., R. G. Roble, E. C. Ridley, and R. E. Dickinson (1990), The Mars thermosphere, II, General circulation with coupled dynamics and composition, *J. Geophys. Res.*, *95*, 14,811–14,827.

Bougher, S. W., S. Engle, R. G. Roble, and B. Foster (1999), Comparative terrestrial planet thermospheres, 2, Solar cycle variation of global structure and winds at equinox, *J. Geophys. Res.*, *104*, 16,591–16,611.

Bougher, S. W., S. Engle, R. G. Roble, and B. Foster (2000), Comparative terrestrial planet thermospheres, 3, Solar cycle variation of global structure and winds at solstices, *J. Geophys. Res.*, *105*, 17,669–17,692.

Brain, D. A., F. Bagenal, M. H. Acuña, and J. E. P. Connerney (2003), Martian magnetic morphology: Contributions from the solar wind and crust, *J. Geophys. Res.*, *108*(A12), 1424, doi:10.1029/2002JA009482.

Cain, J. C., B. Ferguson, and D. Mozzoni (2003), An n = 90 internal potential function of the Martian crustal magnetic field, *J. Geophys. Res.*, *108*(E2), 5008, doi:10.1029/2000JE001487.

Connerney, J. E. P., M. H. Acuña, P. Wasilewski, N. F. Ness, H. Rème, C. Mazelle, D. Vignes, R. P. Lin, D. Mitchell, and P. Cloutier (1999), Magnetic lineations in the ancient crust of Mars, *Science*, *284*, 794–798.

Connerney, J. E. P., M. H. Acuña, N. F. Ness, H. Rème, R. P. Lin, and D. L. Mitchell (2001), The global magnetic field of Mars and implications for crustal evolution, *Geophys. Res. Lett.*, *28*, 4015–4018.

Connerney, J. E. P., M. H. Acuña, N. F. Ness, T. Spohn, and G. Schubert (2004), Mars crustal magnetism, *Space Sci. Rev.*, *111*(1–2), 1–32.

Connerney, J. E. P., M. H. Acuña, N. F. Ness, G. Kletetschka, D. L. Mitchell, R. P. Lin, and H. Rème (2005), Tectonic implications of Mars crustal magnetism, *Proc. Natl. Acad. Sci.*, *102*(42), 14,970–14,975.

Ferguson, B. B., J. C. Cain, D. H. Crider, D. A. Brain, and E. M. Harnett (2005), External fields on the night-side of Mars at Mars Global Surveyor mapping altitudes, *Geophys. Res. Lett.*, *32*, L16105, doi:10.1029/2004GL021964.

Frey, H. V. (2003), Buried impact basins and the earliest history of Mars, paper presented at Sixth International Conference on Mars, Calif. Inst. of Technol., Pasadena, Calif. 20–25 July.

Frey, H. V. (2004), A timescale for major events in early Mars crustal evolution, *Lunar Planet. Sci.*, *XXXV*, abstract 1382.

Frey, H. V., and R. A. Schultz (1988), Large impact basins and the mega-impact origin for the crustal dichotomy on Mars, *Geophys. Res. Lett.*, *15*, 229–232.

Frey, H. V., J. H. Roark, K. M. Shockey, E. L. Frey, and S. E. H. Sakimoto (2002), Ancient lowlands on Mars, *Geophys. Res. Lett.*, *29*(10), 1384, doi:10.1029/2001GL013832.

Head, J. W., M. A. Kreslavsky, and S. Pratt (2002), Northern lowlands of Mars: Evidence for widespread volcanic flooding and tectonic deformation on the Hesperian Period, *J. Geophys. Res.*, *107*(E1), 5003, doi:10.1029/2000JE001445.

Hiesinger, H., and J. W. Head (2004), The Syrtis Major volcanic province, Mars: Synthesis from Mars Global Surveyor data, *J. Geophys. Res.*, *109*, E01004, doi:10.1029/2003JE002143.

Hood, L. L., N. C. Richmond, E. Pierazzo, and P. Rochette (2003), Distribution of crustal magnetic fields on Mars: Shock effects of basin-forming impacts, *Geophys. Res. Lett.*, *30*(6), 1281, doi:10.1029/2002GL016657.

Johnson, C. L., and R. J. Phillips (2005), Evolution of the Tharsis region of Mars: Insights from magnetic field observations, *Earth Planet. Sci. Lett.*, *230*, 241–254.

Lillis, R. J., D. L. Mitchell, R. P. Lin, J. E. P. Connerney, and M. H. Acuña (2004), Mapping crustal magnetic fields at Mars using electron reflectometry, *Geophys. Res. Lett.*, *31*, L15702, doi:10.1029/2004GL020189.

Lillis, R. J., M. Manga, D. L. Mitchell, R. P. Lin, and M. H. Acuña (2005), Evidence for a second Martian dynamo from electron reflection magnetometry, *Lunar Planet. Sci.*, *XXXVI*, abstract 1578.

McEwen, A. S., M. C. Malin, M. H. Carr, and W. K. Hartmann (1999), Voluminous volcanism on early Mars revealed in Valles Marineris, *Nature*, *397*, 584–586.

McGill, G. E. (1989), Buried topography of Utopia, Mars: Persistence of a giant impact depression, *J. Geophys. Res.*, *94*, 2753–2759.

Mitchell, D. L., R. P. Lin, C. Mazelle, H. Rème, P. A. Cloutier, J. E. P. Connerney, M. H. Acuña, and N. F. Ness (2001), Probing Mars' crustal magnetic field and ionosphere with the MGS Electron Reflectometer, *J. Geophys. Res*, *106*, 23,419–23,428.

Mohit, P. S., and J. Arkani-Hamed (2004), Impact demagnetization of the Martian crust, *Icarus*, *168*, 305–317.

Neumann, G. A., M. T. Zuber, M. A. Wieczorek, P. J. McGovern, F. G. Lemoine, and D. E. Smith (2004), Crustal structure of Mars from gravity and topography, *J. Geophys. Res.*, *109*, E08002, doi:10.1029/2004JE002262.

Nier, A. O., and M. B. McElroy (1976), Structure of the neutral upper atmosphere of Mars: Results from Viking 1 and Viking 2, *Science*, *194*, 1298–1300.

Nimmo, F., and M. Gilmore (2001), Constraints on the depth of magnetized crust on Mars from impact craters, *J. Geophys. Res.*, *106*, 12,315–12,324.

Schubert, G., C. T. Russell, and W. B. Moore (2000), Timing of the Martian dynamo, *Nature*, *408*, 665–667.

Schultz, R. A., and H. V. Frey (1990), A new survey of multiring basins on Mars, *J. Geophys. Res.*, *95*, 14,175–14,189.

Smith, D. E., et al. (1999), The global topography of Mars and implications for surface evolution, *Science*, *284*, 1495–1503.

Smith, D. E., et al. (2001), Mars Orbiter Laser Altimeter: Experiment summary after the first year of global mapping of Mars, *J. Geophys. Res.*, *106*(E10), 23,689–23,722.

Sung, K., and J. L. Fox (2000), Electron impact cross sections for use in modeling the ionospheres/thermospheres of the earth and planets, *Eos Trans. AGU*, *80*(48), *Fall Meet. Suppl.*, F931.

Thomson, B. J., and J. W. Head (1999), Utopia basin, Mars: A new assessment using Mars Orbiter Laser Altimeter (MOLA) data, *Proc. Lunar Planet. Sci. Conf. 30th*, abstract 1894.

Voorhies, C. V., T. J. Sabaka, and M. Purucker (2002), On magnetic spectra of Earth and Mars, *J. Geophys. Res.*, *107*(E6), 5034, doi:10.1029/2001JE001534.

Wilson, L., and J. W. Head (1997), Volcanic intrusions on Mars: Heat sources to maintain viable ecosystems?, *Lunar Planet. Sci.*, *XXVIII*, abstract 1086.

M. H. Acuña and J. E. P. Connerney, NASA Goddard Space Flight Center, Greenbelt, MD 20771, USA.

R. J. Lillis, R. P. Lin, and D. L. Mitchell, Space Sciences Laboratory, University of California, 7 Gauss Way, Berkeley, CA 94720, USA. (mitchell@ssl.berkeley.edu)